Optics Communications 282 (2009) 185–197

Contents lists available at ScienceDirect

Optics Communications

journal homepage: www.elsevier.com/locate/optcom

Distributed imaging using an array of compressive cameras

Jun Ke [a,*], Premchandra Shankar [a], Mark A. Neifeld [a,b]

[a] Department of Electrical Computer Engineering, University of Arizona, Tucson, AZ 85721-0104, USA
[b] College of Optical Sciences, University of Arizona, Tucson, AZ 85721-0094, USA

ARTICLE INFO

Article history:
Received 17 February 2008
Received in revised form 31 July 2008
Accepted 24 September 2008

PACS:
42.30.Va
42.30.Wb

Keywords:
Compressive imaging
Feature specific imaging
Sensor networking

ABSTRACT

We describe a distributed computational imaging system that employs an array of feature specific sensors, also known as compressive imagers, to directly measure the linear projections of an object. Two different schemes for implementing these non-imaging sensors are discussed. We consider the task of object reconstruction and quantify the fidelity of reconstruction using the root mean squared error (RMSE) metric. We also study the lifetime of such a distributed sensor network. The sources of energy consumption in a distributed feature specific imaging (DFSI) system are discussed and compared with those in a distributed conventional imaging (DCI) system. A DFSI system consisting of 20 imagers collecting DCT, Hadamard, or PCA features has a lifetime of 4.8× that of the DCI system when the noise level is 20% and the reconstruction RMSE requirement is 6%. To validate the simulation results we emulate a distributed computational imaging system using an experimental setup consisting of an array of conventional cameras.

1. Introduction

Imaging has become an important aspect of information gathering in many defense and commercial applications. Distributed sensor networks are used in many such applications. A sensor network employs a large number of sensors deployed in a distributed fashion [1]. For example distributed imaging sensor networks have been deployed to monitor environmental phenomena [2]. A sensor networks of imaging devices have also been used for applications of event detection [3] and event recognition [4]. Several challenges facing a data- and information-intensive sensor network are identified in Ref. [5]. Those authors argue that "resources including energy, computation, communication, and storage, will remain the key constraints of a sensor node in such networks, with the key reason being the concept of a large number of nodes and the resultant cost requirement". In order to utilize the system resources efficiently, an application-oriented methodology has been proposed to design a smart camera network for the object tracking problem [6]. Conventional high performance cameras have disadvantages for use in sensor networks because of their large size, weight, and associated high operating power cost. In an effort to combat some of these disadvantages Culurciello and Andreou [7] report designs of two customized image sensors with very high dynamic range and ultra-low power operation. Mathur et al. [8] have studied the effect of ultra-low power data storage on the amount of energy consumption in a sensor network. All of these previously reported conventional cameras however, perform the task of capturing images of a scene, and then transmitting all captured data. This approach can lead to inefficient utilization of available bandwidth. Image compression can be used to mitigate these high bandwidth costs at the expense of significant sensor node computation [9]. Energy efficient transmission schemes have been devised using a multiresolution wavelet transform to trade-off image reconstruction quality and sensor node lifetime [10]. A more interesting approach for applications in which the eventual use of imagery is recognition and/or tracking is described in Ref. [11], in which sensor nodes are customized to process the captured images and directly select events of interest from a scene.

In this paper, we propose the deployment of feature specific (FS) imagers [12] in a sensor network. A FS imager as a sensor node has several salient characteristics that are favorable in a resource-constrained imaging sensor network. A FS sensor measures a set of linear projections of an object directly in the optical domain. Therefore it avoids the computational burden of extracting features from a conventional image as a postprocessing step. *FS sensor usually has the number of measurements much smaller than the object dimensionality. Therefore, it can also be considered as a compressive camera.* A FS sensor is a non-imaging sensor because the captured measurements do not visually resemble the object. The resulting linear features (projections) can then be processed for applications such as reconstruction or recognition. Feature specific imaging (FSI) systems have been studied extensively for tasks such as image

* Corresponding author.
E-mail addresses: jke@ece.arizona.edu, junke@email.arizona.edu (J. Ke).

0030-4018/$ - see front matter © 2008 Elsevier B.V. All rights reserved.
doi:10.1016/j.optcom.2008.09.083

reconstruction [12,13], and human face recognition [14]. Several optical implementations of FS sensors have been proposed [15] and the optimal features for minimizing reconstruction error in the presence of noise have been reported [16]. This technique of directly measuring linear projections in the optical domain has also been discussed by researchers in the context of compressive imaging [17,18]. Also many signal/image processing methods have been developed for reconstructing sparse objects from compressed measurements [19–22]. This compression capability of a FS imager suggests that we can reduce the number of measurements and associated processing complexity in a sensor network by employing FS/compressive imagers instead of conventional imagers. Because we measure only those linear projections that are required for achieving a particular task the memory requirement and the transmission cost at each sensor node can be kept low. FSI also provides the potential benefit of increased measurement signal-to-noise ratio (SNR) [12]. These potential advantages make FS sensors attractive alternatives for sensor nodes in a distributed imaging sensor network. Therefore, in this paper, we design a network of FS sensors deployed in a distributed fashion each measuring a unique set of linear features from an object. These linear features could then be processed and transmitted to a base station for reconstructing the object.

The paper is organized as follows: Section 2 mathematically formulates the feature measurements and presents two optical architectures for use in a distributed imaging system. In Section 3 we study the task of object reconstruction and quantify the reconstruction fidelity. We consider measurements based on principal component (PC), Discrete Cosine Transform (DCT), and Hadamard bases. In Section 4, we analyze the energy consumption of our distributed FSI system and compare it with that of a traditional distributed imaging system. Experimental validation of our simulation results are presented in Section 5 before concluding the paper in Section 6.

2. Distributed imaging system framework

2.1. Feature-specific sensor

Fig. 1a presents the schematic diagram of a FS sensor for object reconstruction. Such a sensor contains FS optics and a set of detectors. It measures linear features of the object directly according to a projection basis, e.g., principal component. As a comparison, Fig. 1b presents the schematic diagram of a conventional imager. Such an imager, e.g., a digital camera, measures a noisy isomorphic image of the object.

Feature measurements from a FS sensor can be represented as a system of linear equations

$$\mathbf{y} = \mathbf{F}\mathbf{x} + \mathbf{n} \tag{1}$$

where $\mathbf{x}$, $\mathbf{y}$, and $\mathbf{n}$ represent the object vector of length N, the feature measurement vector of length L, and the additive white Gaussian noise (AWGN) vector of length L, respectively. The projection matrix $\mathbf{F}$ of size $L \times N$ is chosen based on the application. In this paper, we focus on PC, Hadamard, and DCT projections. The projection matrix $\mathbf{F}$ must also satisfy the photon count constraint arising from energy conservation [12]. Including this constraint in Eq. (1), the maximum absolute column sum of the projection matrix should be less than or equal to 1; i.e., $\max_j \sum_i |f_{ij}| \leqslant 1$, where f_{ij} is the element in the ith row and jth column of $\mathbf{F}$. *Most projection matrices consist of both positive and negative elements. We can use a dual-rail optical architecture to measure the positive and negative terms separately followed by subtraction between the two terms to get the desired result. We can also employ a bias to make all projection matrix elements non-negative, which becomes signal dependent and once again can be removed by a subtraction in postprocessing. Both methods cause system performance degradation. The performance degradation from the dual-rail implementation has been discussed in our previous works [12,15]. In this paper, we focus on the DFSI system reconstruction performance using different projection matrices. Therefore we ignore the effect introduced by projection matrix negative elements.*

Multiple candidate FSI architectures have been studied in Ref. [15]. In this paper we consider both the sequential and parallel architectures as shown in Fig. 2. In the sequential FS sensor, L features are measured one by one using a single detector. The total measurement time T_0 is uniformly divided into L time slots for measuring L features. One way to realize these L projection vectors is by using a Digital Micromirror Device (DMD) array as a programmable mask to modulate object irradiance [23]. In this architecture, the measured optical energy depends linearly on the detector's integration time T_0/L. We assume the noise variance per unit bandwidth of the detector and supporting electronics is σ_0^2 and hence the measurement noise variance per feature in the sequential architecture is $L\sigma_0^2/T_0$. In a parallel architecture FS sensor, L features are collected during the same time period T_0. Note that, the number of detectors used in the parallel architecture is L. Each detector makes one feature measurement. One example of implementing a parallel FS sensor is by using an array of lenses and amplitude masks [15]. Because the sensor's pupil is divided uniformly into L smaller pupils, the object irradiance collected in each feature measurement is reduced by a factor L. However the detector noise variance is σ_0^2/T_0 because the bandwidth of the detector and supporting

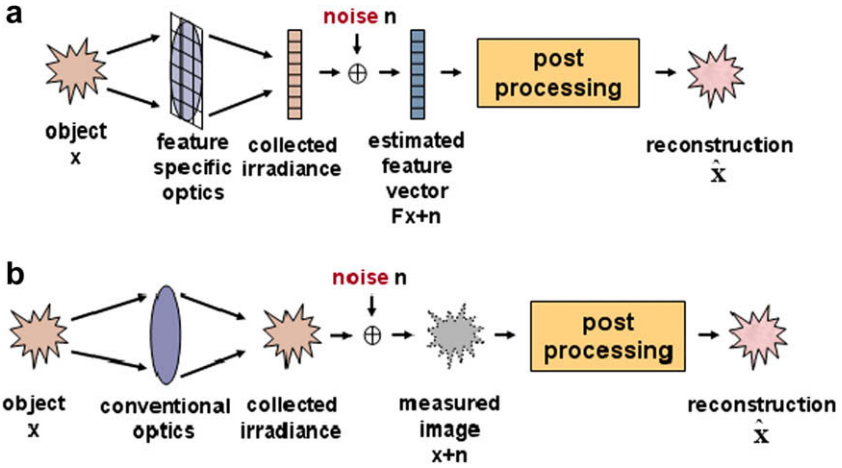

Fig. 1. Schematic diagrams of (a) a feature-specific imager and (b) a conventional imager.

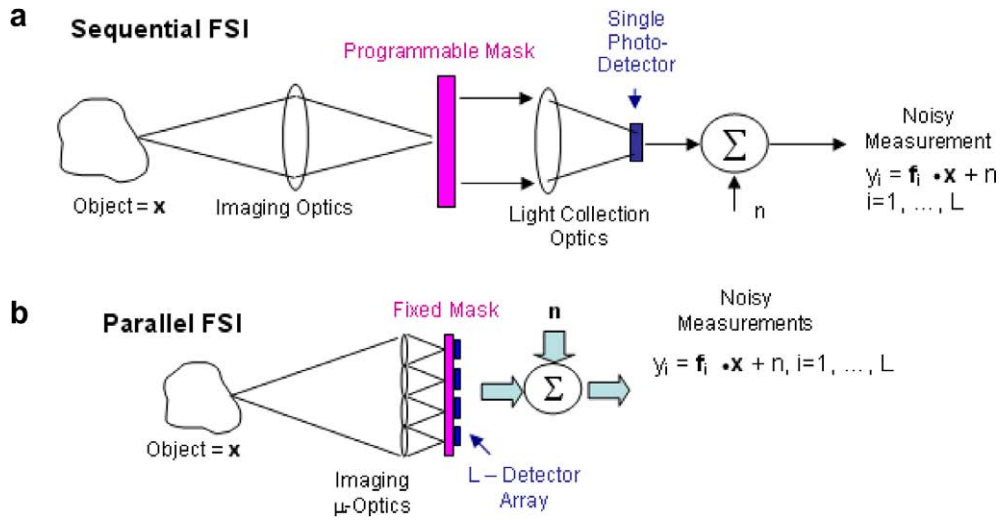

Fig. 2. Two implementations of a feature-specific imager using (a) sequential and (b) parallel architectures.

electronics is $1/T_0$. Comparing the two architectures, the noise variance in the sequential architecture is L times larger than that in the parallel architecture. Therefore, we expect that the distributed FSI (DFSI) system using a parallel architecture will provide better performance than the sequential architecture.

In a conventional imager, optical resolution is often determined using the diffraction limit of the imaging optics and the camera's sensor pixel size. However, in a FS sensor the concept of resolution is not well-defined. The FS sensor makes non-conventional projective measurements as shown in Fig. 1a. Therefore the FS detector size does not have any direct impact on reconstruction resolution, hence we do not define the measurement resolution. The reconstruction resolution depends on the optics between the scene and the mask, the mask pixel size, and the number of feature measurements L. In this paper, we assume that this resolution is matched to the desired object pixel size.

2.2. Distributed Imaging System

Fig. 3 presents the schematic diagrams of two distributed imaging systems, each with K sensor units. A distributed conventional imaging (DCI) system consisting of conventional imagers is shown in Fig. 3a. Each imager makes N measurements. Fig. 3b presents a DFSI system consisting of FS sensors. *Each sensor makes $L \ll N$ measurements. Therefore a total of, $M = L \times K$ features are measured in a DFSI system with K sensors. A sequential architecture DFSI system consists of K detectors, because features are measured one after the other by the single detector in each sensor. A parallel architecture DFSI system consists of M detectors. Each sensor has L detectors to make feature measurements during the same time period.* In both DCI and DFSI systems, sensor units send the measurements to a base station after some processing e.g. data compression. To simplify the problem, we assume that the distance from object to sensor is large and that the distances from different sensors to the base station are approximately the same. However, the geometry of sensors must be taken into consideration during the design of the DFSI system and during the postprocessing in a DCI system. Consider the DCI system as an example. Because each imager in the array of conventional imagers will have different positions and orientations, the measured images will have different rotation angles, magnifications, and translations. We choose one sensor as the reference.

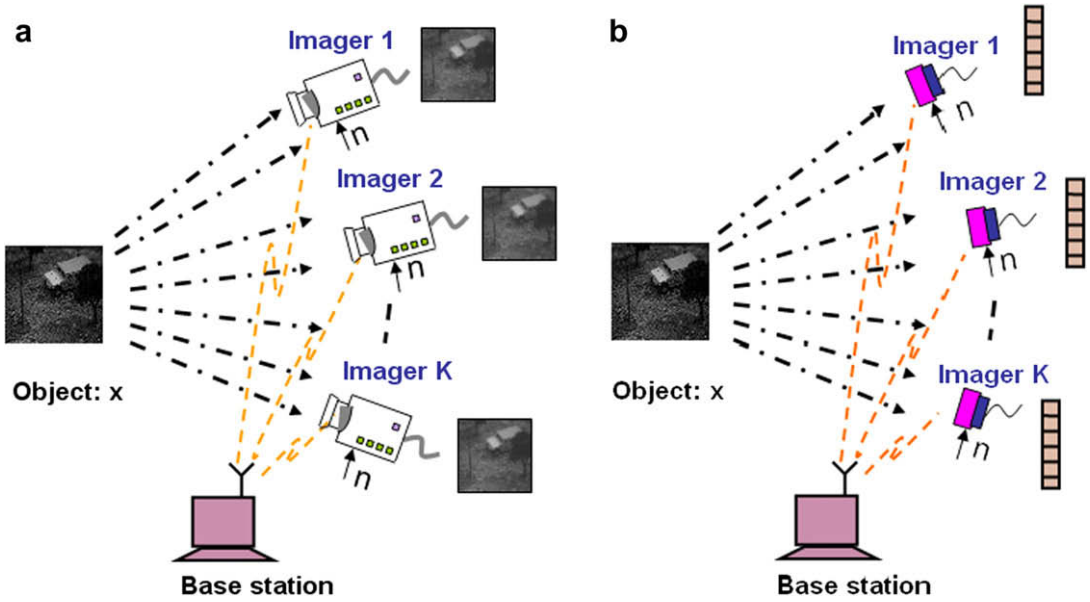

Fig. 3. Schematic diagrams of (a) a distributed imaging system using conventional imagers (DCI), and (b) a distributed imaging system using feature-specific imagers (DFSI). The imagers in DCI measure different views of an object, whereas the imagers in DFSI measure different linear projections of the object.

Then the geometry of the kth sensor with respect to the reference can be represented by a geometric transformation matrix $\mathbf{G}_k$. To compensate for these geometric effects in a DFSI system, the same geometric transformation is applied to the projection vectors during the system design and/or deployment. For example, in a DFSI system the feature measurements $\mathbf{y}_k$ for the kth sensor can be written as

$$\mathbf{y}_k = (\mathbf{G}_k\mathbf{F}_k^T)^T\mathbf{G}_k\mathbf{x} + \mathbf{n}_k \qquad \Rightarrow \qquad \mathbf{y}_k = \mathbf{F}_k\mathbf{x} + \mathbf{n}_k \tag{2}$$

where $\mathbf{G}_k$ is the $N \times N$ matrix representing the geometry of the kth imager, $\mathbf{F}_k$ is the $L \times N$ projection matrix required for measuring features in the kth imager, and $\mathbf{n}_k$ is the L dimensional measurement noise vector at the kth imager. In the next section, we discuss different types of $\mathbf{F}_k$, a method to obtain an object estimate from the set of $\{\mathbf{y}_k, k = 1, 2, \ldots, K\}$, and the reconstruction fidelity of the resulting object estimates.

3. Reconstruction fidelity: simulation and analysis

We use the linear minimum mean squared error (LMMSE) estimation to reconstruct the object in a DFSI system. The LMMSE estimate is given by $\hat{\mathbf{x}} = \mathbf{W}\mathbf{y}$, where $\mathbf{W}$ is the Wiener operator defined as

$$\mathbf{W} = \mathbf{R_x}\mathbf{F}^\mathbf{T}(\mathbf{F}\mathbf{R_x}\mathbf{F}^\mathbf{T} + \mathbf{D_n})^{-\mathbf{1}} \tag{3}$$

$\mathbf{R_x}$ and $\mathbf{D_n}$ are the object and noise autocorrelation matrices, respectively. Reconstruction fidelity is evaluated using of the root mean squared error $RMSE = \sqrt{E\{\frac{|\mathbf{x}-\hat{\mathbf{x}}|^2}{N}\}}$ where E is the ensemble average over many objects. *Our fundamental object size is* 32×32. *We derive 1024-dimension projection vectors to work with the fundamental object. However for training purpose we employ two hundred* 256×256*-pixel objects. In such case* 32×32-pixel overlapping blocks are gathered from these training objects and used to estimate $\mathbf{R_x}$. *To measure features from a larger object we assume that the object is segmented into non-overlapping* 32×32*-pixel blocks, and each* 32×32*-pixel block is treated independently as a fundamental object. For example, in a sequential architecture DFSI system, we require 64 detectors to measure features from a* 256×256*-pixel object. Each detector collects the light from an object block after it is spatially modulated by the mask. Detector noise is still the dominant measurement noise. Noise energy per feature is still* σ_0^2/T_0 *and* $L\sigma_0^2/T_0$ *in parallel and sequential architecture DFSI systems, respectively.*

In Figs. 4 and 5, the variation of RMSE is plotted vs. the number of features M, for various numbers of sensors K and noise variances of $\sigma_0^2 = 0.1$ and 0.0025, respectively. A set of objects that are different from the training objects is used here. The parallel and sequential architectures are represented by solid and dotted lines, respectively. From Figs. 4 and 5 we make the following observations. First, it is clear that a DFSI system using the parallel architecture provides smaller RMSE compared with the sequential architecture. Second, each RMSE curve has a minimum value at some M. To understand this observation, we notice that there are two error components in reconstruction: truncation error and measurement error. Truncation error comes from insufficiently representing a N-dimensional object in the $M = L \times K$-dimensional feature space, where $M < N$. Notice that the truncation error is reduced by using more features for reconstruction. The measurement error comes from the residual noise after LMMSE operator. This error is larger when more features are used for reconstruction because of reduction in measurement SNR [15]. Truncation and measurement errors trade-off optimally at the

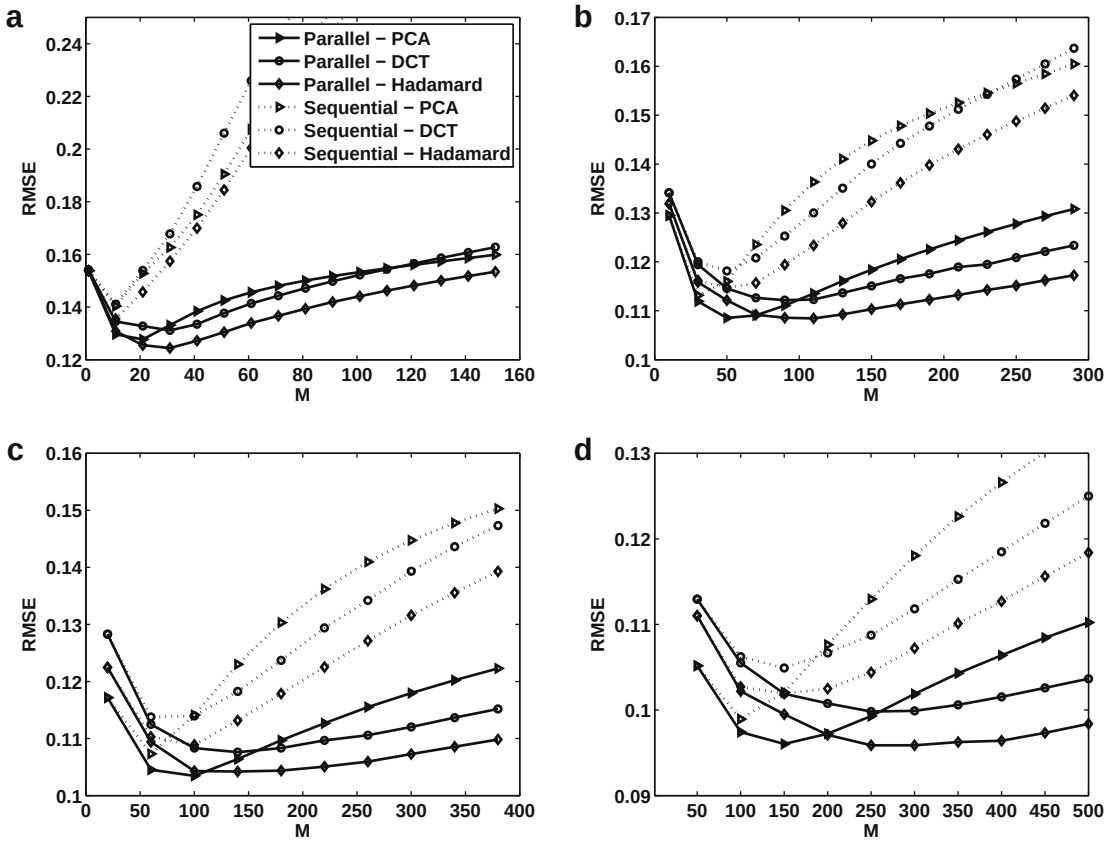

Fig. 4. Plots of reconstruction RMSE versus the number of features M collected by sensor network using (a) $K = 1$, (b) $K = 10$, (c) $K = 20$, and (d) $K = 50$ feature-specific imagers. The noise variance is $\sigma_0^2 = 0.1$.

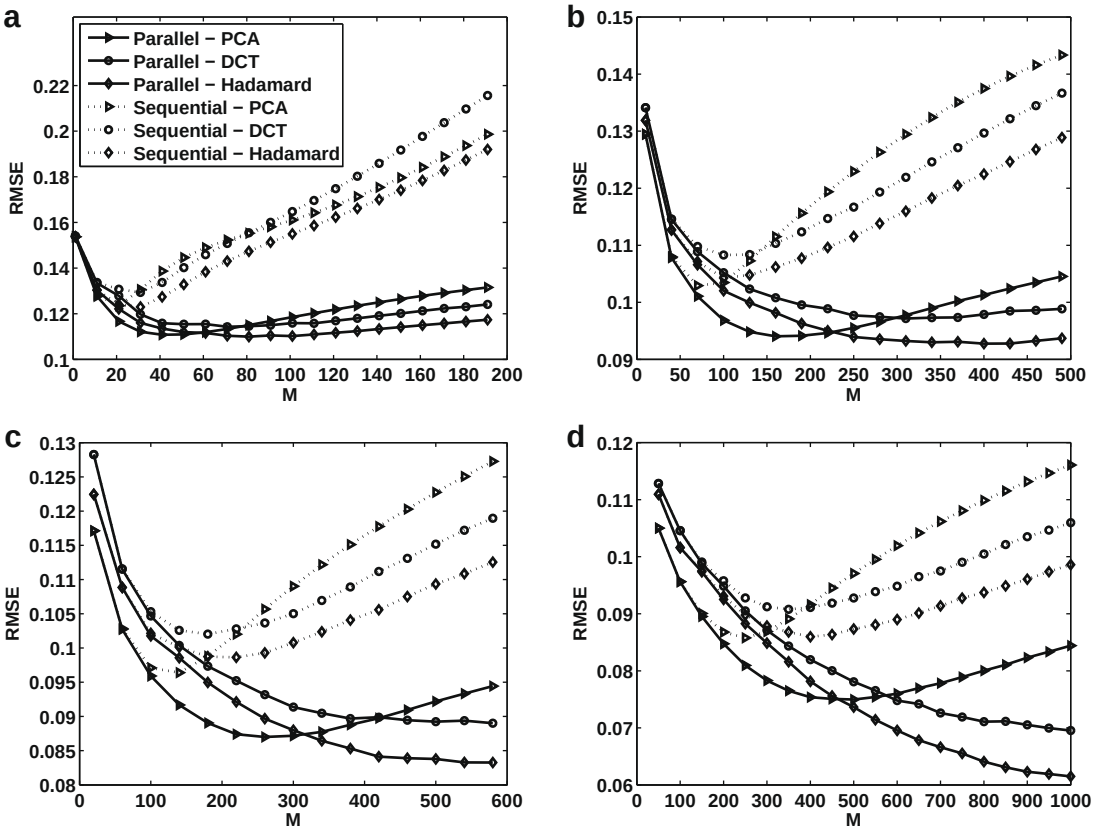

Fig. 5. Plots of reconstruction RMSE versus the number of features M collected by sensor network using (a) $K = 1$, (b) $K = 10$, (c) $K = 20$, and (d) $K = 50$ feature-specific imagers. The noise variance is $\sigma_0^2 = 0.0025$.

minimum RMSE point. The third observation is that compared with the DCT and Hadamard bases, the PCA basis achieves smaller RMSE value when M is small. For example, the RMSE values using PCA, Hadamard, and DCT features are 0.0974, 0.1022, and 0.1055, respectively when $M = 100$, $K = 50$, and $\sigma_0^2 = 0.1$. Because the PCA bases are derived from $\mathbf{R_x}$ which corresponds to object prior knowledge, they can yield smaller truncation error and RMSE when M is small (i.e., when truncation error dominates). This also means that the PCA projection achieves its minimum RMSE value using a smaller M value. However, when M is large, reconstruction using the Hadamard features has smaller RMSE. For example, the RMSE values using PCA, Hadamard, and DCT features are 0.1102, 0.0984, and 0.1036, respectively when M is increased to 500, and keeping $K = 50$, and $\sigma_0^2 = 0.1$. Because measurement error dominates RMSE when M is large, it is more critical to increase the signal energy (hence the measurement SNR) than to use a basis with a good data compaction property. Collecting more photons requires that all column sums of $\mathbf{F}$ be made close to 1 after normalization in order to minimize photon loss. The Hadamard basis satisfies this requirement, and hence the Hadamard based DFSI system has smaller measurement error with large M. We also observe that the minimum reconstruction RMSE reduces with increasing number of imagers, K. For example from Fig. 4 we notice that the minimum RMSE decreased from 0.124 to 0.095 when K is increased from 1 to 50 in case of parallel Hadamard implementation. In fact this trend holds when K is increased for a fixed M. *Fig. 6 presents examples of an object and some reconstructions. The projection method is PCA, the number of imagers K = 10, and noise variance* $\sigma_0^2 = 0.0001$. *The RMSE values obtained from the sequential architecture DFSI system are 0.1108 and 0.1233 for M = 200 and 500, respectively. These values are higher than the RMSE values obtained from the parallel architecture DFSI system, which are 0.1027 and 0.0867 when M = 200 and 500, respectively.*

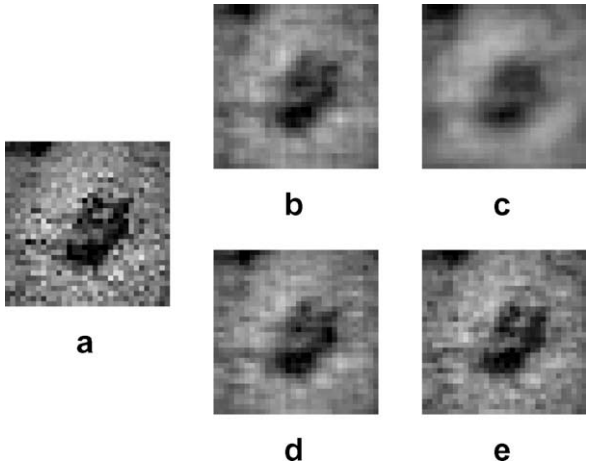

Fig. 6. Example reconstructions using PCA projections from $K = 10$ number of imagers at noise level of $\sigma_0^2 = 0.0001$. (a) Object of size 32×32. Reconstructions using sequential architecture with (b) $M = 200$, and (c) $M = 500$ features. Reconstruction using parallel architecture with (d) $M = 200$, and (e) $M = 500$ features.

We extract the minimum RMSE values from Figs. 4 and 5 and plot them as a function of noise variance in Fig. 7. The following observations are based on Fig. 7. 1) As expected, the parallel DFSI system exhibits better RMSE performance at all noise levels. 2) When the noise level is high, reconstruction using the PCA and Hadamard features provide similar RMSE performance. 3) When the noise level is small, e.g., $\sigma_0^2 < 10^{-6}$ and $K = 50$ as in Fig. 7d, reconstruction using the PCA basis has slightly smaller RMSE,

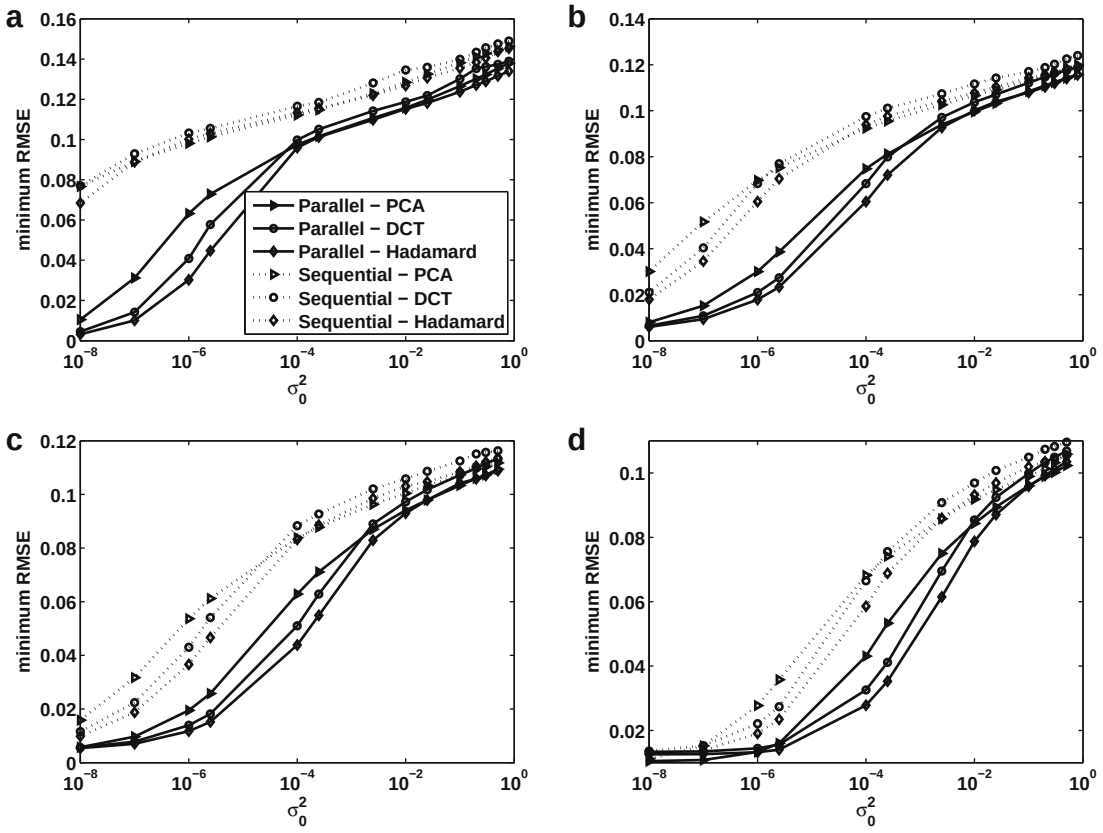

Fig. 7. Minimum reconstruction RMSE versus the noise variance σ_0^2 for sensor network with (a) $K = 1$, (b) $K = 10$, (c) $K = 20$, and (d) $K = 50$ feature-specific imagers.

because the PCA is optimal in the absence of noise. 4) When the noise level is in the moderate range, the Hadamard basis provides smaller minimum RMSE. As described before, this is because on average more object photons will be collected using Hadamard features. Therefore, making more Hadmard feature measurements will reduce the truncation error with minimal increase in the measurement error.

Next we examine the optimal number of features M_{opt} required to achieve the minimum RMSE. Fig. 8 plots M_{opt} as a function of K for three different noise levels $\sigma_0^2 = 0.8$, 0.01, and 0.0025. PCA, Hadamard, and DCT features are studied. Only the parallel DFSI architecture is discussed here onwards because of its superior RMSE performance. From Fig. 8, it is clear that M_{opt} increases with increasing K or decreasing σ_0^2. This is because increasing K and/or

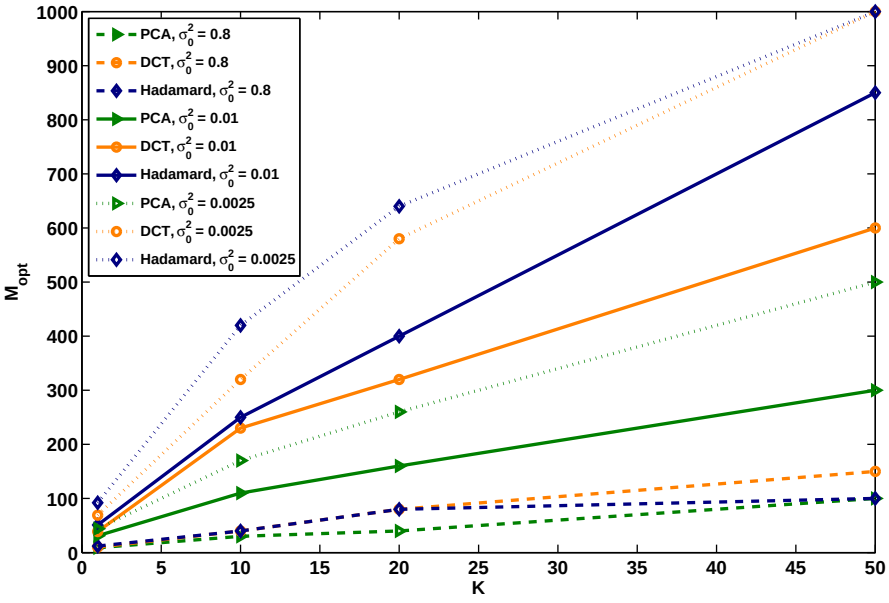

Fig. 8. The number of features generating minimum RMSE, M_{opt}, versus the number of imagers in a DFSI sensor network, K. Data is shown for three noise levels σ_0^2 = 0.8, 0.01, and 0.0025.

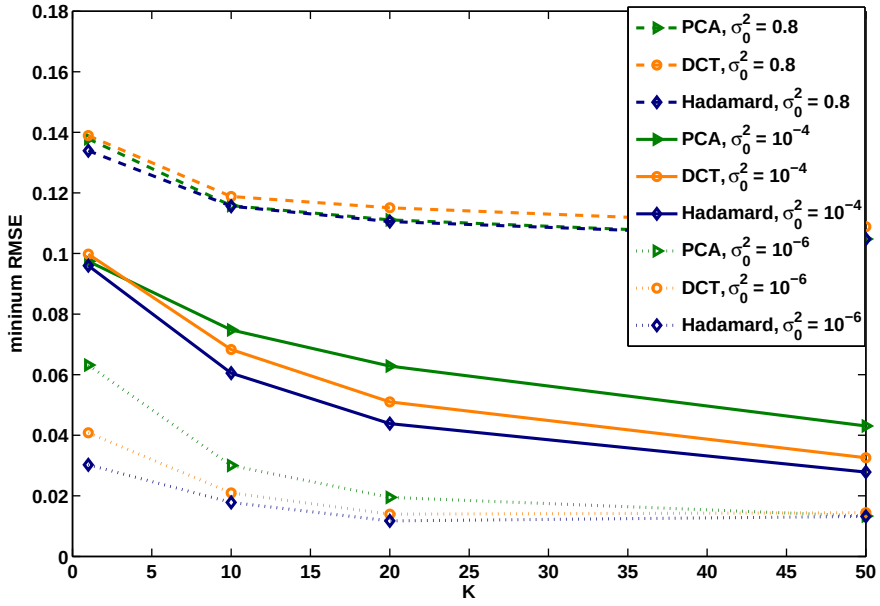

Fig. 9. Minimum reconstruction error versus the number of imagers K in a DFSI sensor network. Data is shown for three noise levels $\sigma_0^2 = 0.8$, 10^{-4}, and 10^{-6}.

reducing σ_0^2 improves the measurement SNR. When measurement SNR increases, a larger number of features can be measured before balance of noise and truncation error is reached. Fig. 8 also demonstrates that Hadamard basis vectors generally require the largest M_{opt} values to achieve minimum RMSE.

The last aspect of DFSI reconstruction performance is the impact of the number of imagers K on reconstruction quality. Fig. 9 presents the minimum RMSE versus K for high, moderate, and low noise levels using PCA, DCT, and Hadamard features. As expected, the minimum RMSE decreases as more FS imagers are used and/or as the detector noise level σ_0^2 is reduced.

4. System lifetime: simulation and analysis

In this section we quantify the lifetime of a distributed imaging system by calculating its energy consumption. The system lifetime is expected to be short when the energy consumption is high, and vice-versa. We define the DFSI system lifetime as the maximum time period before *any* one FS imager runs out of battery. This definition is sensible because in a DFSI system, all sensors work in collaboration to measure the scene. In a DCI system on the other hand, at any given time only one conventional imager is assumed to be in the active mode for measuring, compressing, and transmitting data. After one such imager runs out of battery, another imager is turned on. Therefore the DCI system lifetime is the time period before *all* imagers run out of battery.

Three processes dominate the energy consumption in a distributed imaging system: the energy used for (1) measurement E_{meas}, (2) on-board processing/data compression E_{proc}, and (3) communication E_{comm}. We calculate these three energy components by considering commercially available electronics and optical devices for the proof of concept. The power consumption details of these devices are discussed in the Appendix. Summing up all three values E_{meas}, E_{proc}, and E_{comm} gives the total energy consumption for one imager. Then, the lifetimes of DCI and DFSI systems are defined as

$$\text{DCI Lifetime} = \frac{E_b}{E_{conv}} \times K \quad (round) \tag{4}$$

$$\text{DFSI Lifetime} = \frac{E_b}{\max_k\{E_{FS}^k\}} \quad (round) \tag{5}$$

where E_b is the sensor battery energy, E_{conv} is the energy consumption for one conventional imager, and E_{FS}^k is the total energy consumption for the kth FS sensor. *We assume that in each time unit sensors measure, process, and send data back to the base station for single object. In our study, we use a previously defined time unit of round to quantify the system lifetime [24].* We assume that one *Energizer* 186 button cell battery is used for the sensor power supply. It can provide roughly 500 J of energy before its working voltage drops below the cut-off value 0.9 V.

We use 7 objects of size 480 × 640-pixels to evaluate DFSI and DCI energy consumption. They are processed block-wise using 32 × 32-pixel blocks as described in Section 3. Both systems have $K = 20$ imagers. We consider the noise level of $\sigma_0^2 = 0.04$.

Note that an important part of the on-board processing is the compression of the measurements before sending them to the base station. Fig. 10 presents the compression protocol used in our DFSI system. The details of the protocols used in both systems are included in the Appendix. Here we elaborate on the effect of quantization on the DFSI reconstruction process. The measured features

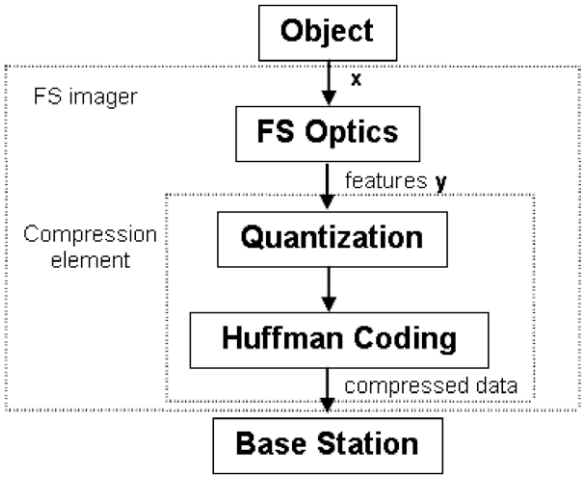

Fig. 10. Compression protocol used for FS imagers. The quantization table is different for different types of measured features.

are scaled using a quantization table and rounded up to the nearest integers. Therefore the quantization introduces a third reconstruction error – quantization error into the system. For simplicity, we assume quantization error is independent of the feature measurements and the detector noise. Therefore, the Wiener operator may be modified as

$$\mathbf{M} = \mathbf{R_x F^T}(\mathbf{F R_x F^T} + \mathbf{R_{qn}} + \mathbf{D_n})^{-1} \quad (6)$$

where $\mathbf{R_{qn}}$ is the auto-correlation matrix of the quantization error. The quantization error level can be controlled by scaling the quantization table elements with a factor q. Large q values introduce large quantization error. Fig. 11 presents the RMSE vs. M for cases in which measured Hadamard features are compressed using $q = 4$ and $q = 10$. As expected the RMSE obtained using a small q value is approximately equal to the RMSE using non-compressed features. A larger value of q introduces a larger degradation in reconstruction RMSE. For example reconstruction from $M = 200$ Hadamard features compressed using $q = 10$ has 5% higher RMSE than that from as many compressed features using $q = 4$. Fig. 12b and c show sample reconstructions for $q = 30$ using 260 non-compressed and compressed Hadamard features, respectively, for the object in Fig. 12a. These reconstructions have RMSE values of 0.0365 and 0.0467, respectively. The reconstruction in Fig. 12c is visually similar to the reconstruction using non-compressed features in Fig. 12b. Reconstructions using compressed PCA and DCT features will also have higher RMSE compared to reconstructions using uncompressed features.

The energy requirement of the system is determined by the amount of data measured and processed. The requirement is high when M is large and/or q is small because of the large amount of data. Table 1 lists E_{meas}, E_{proc}, and E_{comm} in a PCA based DFSI system for $q = 4$, 30 and $M = 100$, 500, and 900. As expected, when M increases all three energy consumptions increase. E_{proc} and E_{comm} are larger for $q = 4$ than those for $q = 30$. E_{meas} doesn't change by varying q because E_{meas} depends only on M. Note that E_{comm} is dominant among the three components for all M and q values as we assumed a relatively large distance from sensors to base station. This is similar to the observations made in Ref. [25].

From the above analysis, it is clear that both M and q affect both the reconstruction fidelity and energy consumption. For a given feature basis, a fixed number of FS imagers, and a fixed standard deviation of noise, each (M,q) pair is associated with a pair of performance metrics: reconstruction RMSE and system lifetime.

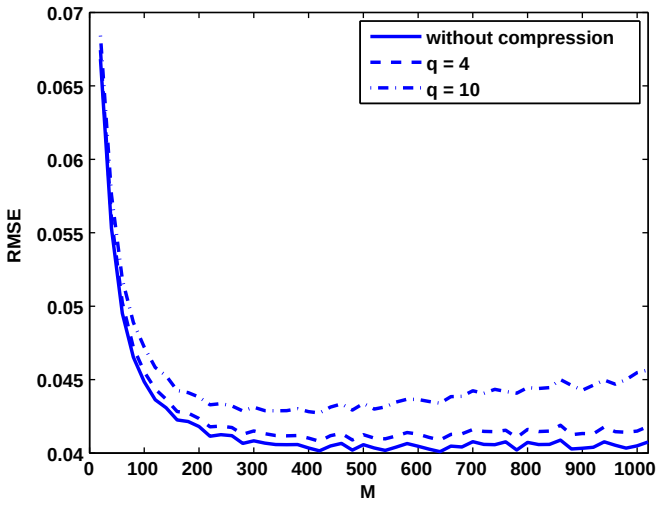

Fig. 11. RMSE vs M using compressed and non-compressed Hadamard features for $K = 20$ FS imagers at a noise level $\sigma_0^2 = 0.04$.

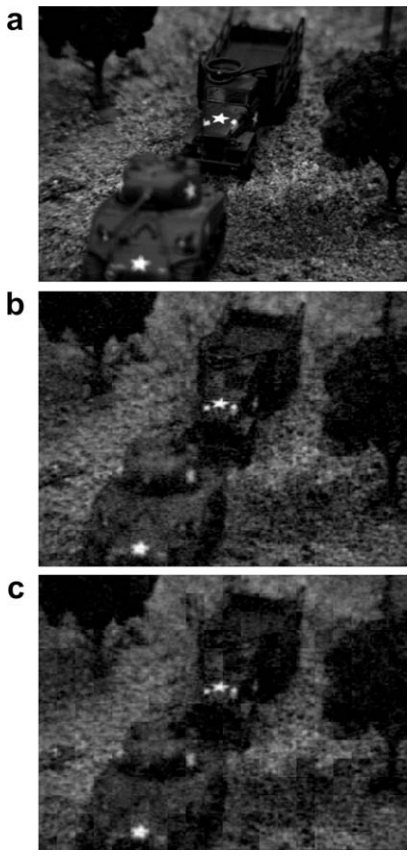

Fig. 12. Example of (a) original object, and reconstruction from $M = 260$, (b) non-compressed Hadamard features, and (c) compressed Hadamard features for $q = 30$ using $K = 20$ FS imagers at a noise level $\sigma_0^2 = 0.04$.

Table 1
Energy consumption components for PCA based DFSI systems for $\sigma_0^2 = 0.04$ and $q = 4,30$.

M	100		500		900	
q	4	30	4	30	4	30
E_{comm}(mJ)	1242.5	629.4	4722.9	2200.8	7990.4	3643.0
E_{meas}(mJ)	0.806	0.806	4.031	4.031	7.256	7.256
E_{proc}(mJ)	0.006	0.006	0.032	0.022	0.056	0.036

Fig. 13 presents system lifetime vs. RMSE for different (M,q) values for a PCA based DFSI system having $K = 20$ FS imagers and a noise level $\sigma_0^2 = 0.04$. We observe that for a fixed q, increasing M decreases the reconstruction RMSE. However, it reduces the system lifetime because of the higher energy requirement for processing more data. For fixed M, e.g. $M = 20$, when q increases from 4 to 30, quantization error increases and thus RMSE increases. However the system lifetime is larger because feature data are more compressed using larger q. Another observation from Fig. 13 is that many (M,q) values achieve a given RMSE requirement but have different system lifetimes. We choose the (M,q) values having the maximum system lifetime. Fig. 14 plots system lifetime vs. the reconstruction RMSE for the optimal (M,q) values in PCA, Hadamard, and DCT based DFSI systems. The number of imagers is $K = 20$ and the noise variance is $\sigma_0^2 = 0.04$. We observe that the PCA based DFSI system has the largest system lifetimes over all RMSE requirements. The lifetime of a corresponding DCI system is also plotted as a function of RMSE in Fig. 14. It is clear that the DFSI systems have larger lifetime values than the DCI system. For example, when RMSE requirement is 0.0592, the PCA, Hadamard and DCT based DFSI systems have 4.8, 3, and 2.4 times the lifetime of the DCI

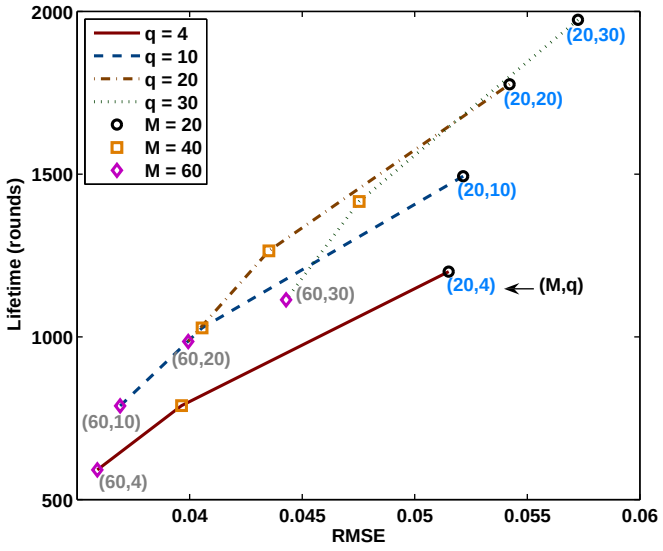

Fig. 13. Lifetimes of PCA based DFSI system with noise level $\sigma_0^2 = 0.04$ for different (M,q)).

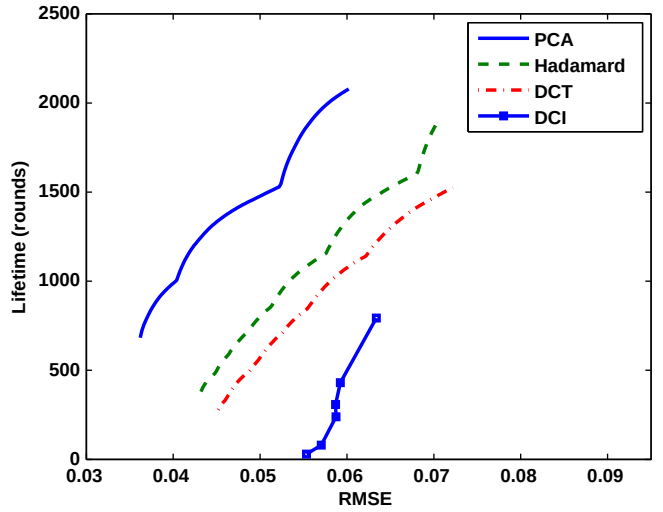

Fig. 14. Lifetimes of DCI system and DFSI system using PCA, DCT and Hadamard features with noise level $\sigma_0^2 = 0.04$ when (M,q) is optimized.

system, respectively. More imagers can be used to further improve the DFSI system lifetime.

5. Experiment

We used a conventional distributed imaging setup in order to validate the simulation results obtained from our DFSI system model. Fig. 15 shows a snapshot of the experimental setup. The plasma monitor is used to display an object at a distance of about 1.5 m from an array of Firewire-based web-cameras and images with different views of the object are captured. *The cameras are placed at the same distance from the object and an affine geometry is assumed for their deployment. The rotation, magnification, and translation parameters of each camera are determined during the system calibration. A grid patterned image is shown on the monitor as a calibration object. The camera parameters are estimated by matching the image with respect the reference image. The image calibration is performed by choosing a set of corresponding points in the image to be aligned and reference image [26]. The difference between the reference and the calibration result is very small.* The process of feature measurement is emulated numerically using these measured images. These features are further corrupted by additive white Gaussian noise. We consider PCA, DCT, and Hadamard features assuming the parallel FSI architecture. The noise variance is $\sigma_0^2 = 0.09$. In Fig. 16 we plot RMSE vs. M using $K = 2,3$, and 4 imagers and a 128×128-pixel object. As mentioned in Section 3, we process the object as a set of 32×32-pixel blocks. *For each block we make $L = M/K$ feature measurements.* With accurate knowledge of all camera geometries, the experimental RMSE curves can be expected to behave in the same way as did the simulation RMSE curves. From Fig. 16 we observe that the reconstruction RMSE reduces with increasing K. The experimental data also exhibits a minimum RMSE at M_{opt}. The optimal number of features at which this minimum is achieved increases with increasing K as shown in Table 2. The table also lists the minimum RMSE values and the M_{opt} values obtained by using only one captured image and simulating the remaining images by numerically performing the geometric transformations. We find that the minimum RMSE values match very well and that the experimental system generally requires a few more features to achieve the same RMSE. Some example reconstructions using PCA and Hadamard features are shown in Fig. 17. Fig. 17a and e show images captured using two conventional cameras from which FSI performance is emulated. The images in Fig. 17b–d are reconstructed using 36 PCA features from $K = 2$, 3, and 4 cameras, respectively. They have RMSE values of 0.119, 0.111, and 0.105, respectively. The images in Fig. 17f–h are reconstructed using 120 Hadamard features using $K = 2$, 3, and 4 cameras, respectively. These images have RMSE values of 0.151, 0.136, and 0.126, respectively. As K increases both the RMSE and the visual quality of reconstructions improve. *As we discussed in the previous section, the resolution concept is not well-defined in DFSI system. We assume that the optical resolution is matched to the desired object pixel size.*

Fig. 15. A snapshot of DFSI experimental set-up.

We extend our experiments to include evaluations of energy consumption and lifetime as explained in Section 4. Fig. 18 shows reconstruction RMSE versus the total number of features using $K = 5$ imagers with compressed and uncompressed PCA, Hadamard, and DCT features. In the case of compression we used a quantization table with a scaling factor $q = 10$. We observe that compression degrades the reconstruction fidelity. For example the reconstruction RMSE increases by 7.8%, 11.4%, and 19.4% due to compressing 200 DCT, Hadamard, and PCA features, respectively. Next we quantify the lifetime of the system. Because there are many (M,q) values that achieve a required reconstruction RMSE we conduct an exhaustive search to find the optimal pair for each RMSE. Fig. 19 plots DFSI system lifetime obtained by using the

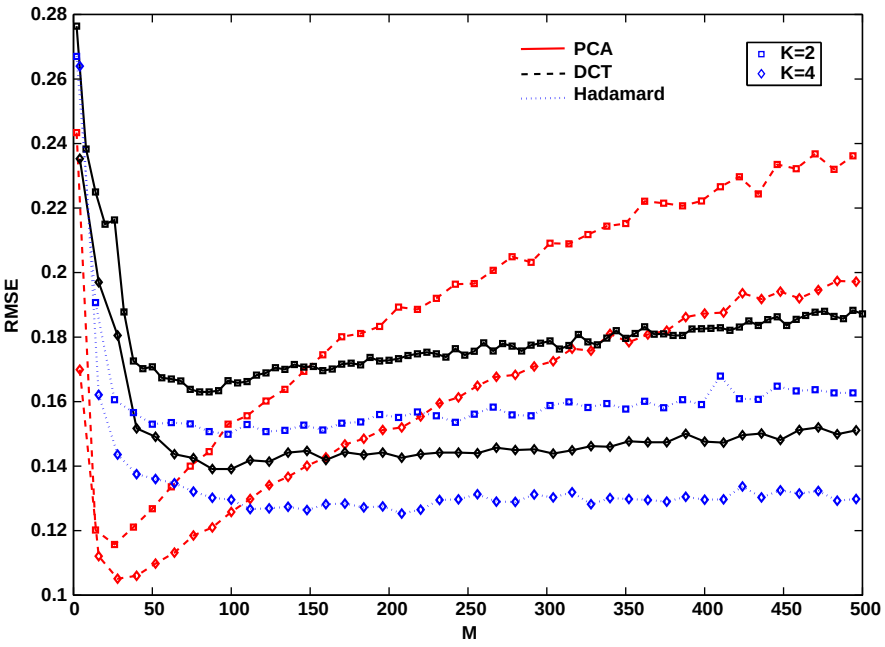

Fig. 16. The reconstruction RMSE versus the total number of PCA features and Hadamard features using $K = 2$, 3, and 4 cameras. The noise variance is $\sigma_0^2 = 0.09$.

Table 2
M_{opt} for $K = 2,3,4$ using PCA, Hadamard, and DCT features.

	Simulation						Experiment					
	PCA		Hadamard		DCT		PCA		Hadamard		DCT	
	min RMSE	M_{opt}	min RMSE	M_{opt}	min RMSE	M_{opt}	min RMSE	M_{opt}	min RMSE	M_{opt}	min RMSE	M_{opt}
$K = 2$	0.114	22	0.150	114	0.163	86	0.114	22	0.150	98	0.163	88
$K = 3$	0.108	22	0.134	117	0.150	87	0.109	30	0.136	135	0.150	90
$K = 4$	0.104	22	0.125	124	0.140	92	0.104	32	0.126	164	0.140	98

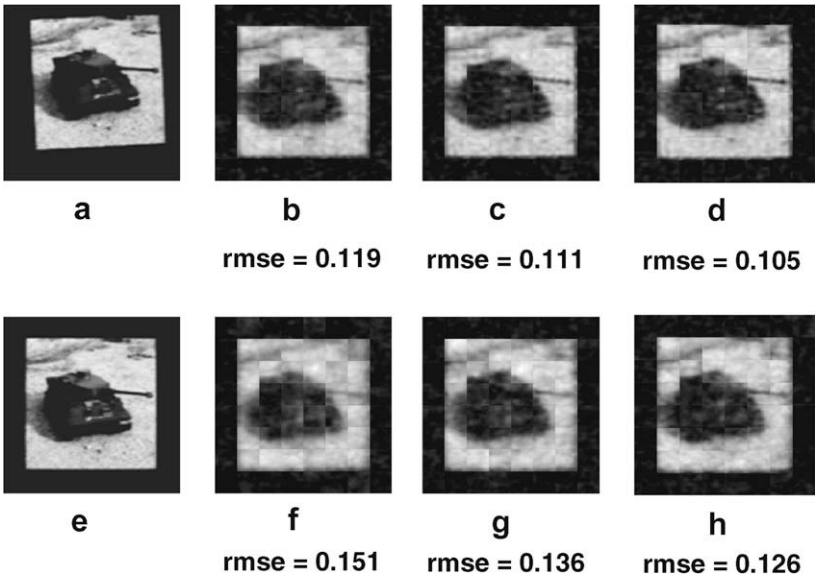

Fig. 17. Example reconstructed images. Images obtained from two conventional cameras are shown in (a) and (e). The images in (b), (c), and (d) are reconstructed using 36 PCA features and $K = 2$, 3, and 4 cameras, respectively. The images in (f), (g), and (h) are reconstructed using 120 Hadamard features and $K = 2$, 3, and 4 cameras. The noise variance $\sigma_0^2 = 0.09$.

optimal (M, q) values versus the achieved reconstruction RMSE for $K = 5$ imagers. We also compare the lifetimes of DFSI systems using Hadamard, PCA, DCT with that of a corresponding DCI system. The DFSI system measuring PCA features has the highest lifetime for a fixed reconstruction RMSE because of its lowest energy requirement to achieve given reconstruction fidelity. The DCT and Hadam-

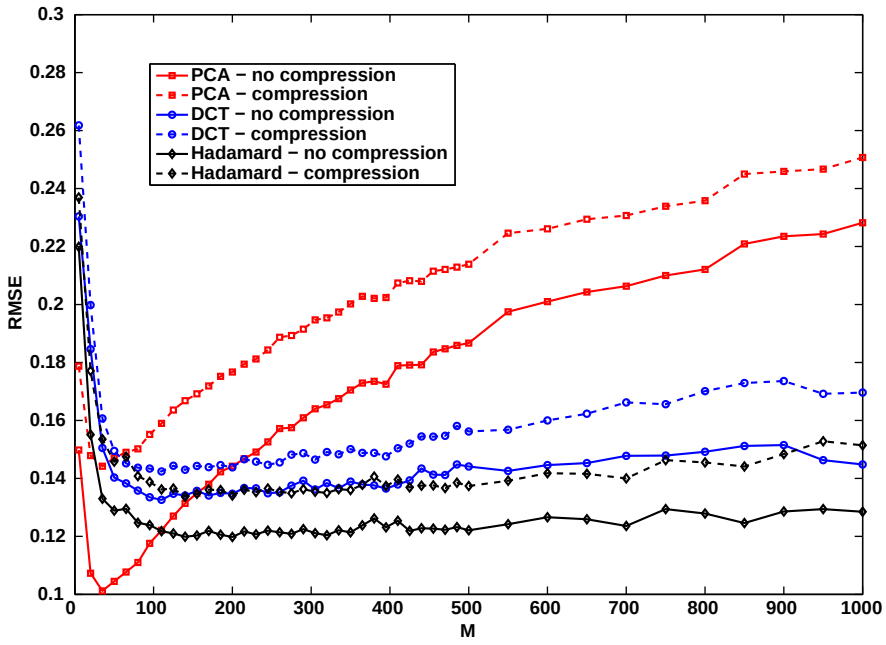

Fig. 18. RMSE versus the total number of features M with or without compressing PCA, DCT, and Hadamard features. The number of cameras $K = 5$ and noise variance $\sigma_0^2 = 0.09$. The compression scaling factor $q = 10$.

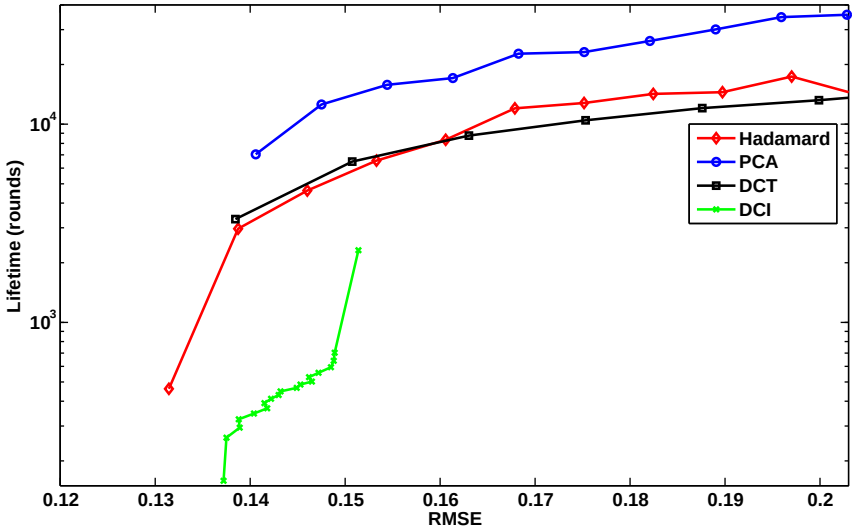

Fig. 19. Lifetimes of DCI system and DFSI systems using Hadamard, PCA, and DCT features versus the achieved reconstruction RMSE. The optimal (M,q) pair is chosen at every RMSE. The number of imagers $K = 5$ and the noise variance $\sigma_0^2 = 0.09$.

Table 3
Energy consumption components for DCI and DFSI systems.

		DCI	DFSI
Feature measurement	Equipment	OmniVision OV7141	Thorlab DET10A & TLC1541
	E_{meas}	1.3 mJ/sensor	$0.5375L\mu$J/sensor
On-board process	Equipment	ARM7TDMI	ARM7TDMI
	E_{comp}	$(1100N + 4000N\xi)$ pJ/sensor	$(200L + 4000\alpha)$ pJ/sensor
Transmission	E_{comm}	$100,050\gamma$ nJ/sensor	$100,050\gamma$ nJ/sensor

* N is the number of object pixels; L is the number of features for each sensor; ξ is the compression quality; α is the number of non-zeros coefficients after compression; γ is the amount of transmission data in bits.

ard features yield almost the same lifetime. The lifetimes of DFSI systems using PCA, Hadamard, and DCT features are 20.2×, 8.4× and 7.2× higher than the lifetime of DCI system, respectively at RMSE of 0.149.

6. Conclusion

In this paper we present the concept of a distributed imaging system that consists of FS imagers to collect data for object reconstruction. We consider PCA, Hadamard, and DCT features using either the sequential or the parallel optical implementation schemes. Reconstruction fidelity quantified using RMSE, is

analyzed for systems with different numbers of imagers (K) for measuring different total numbers of features (M) at several measurement noise levels, σ_0. We observe that the parallel architecture provides better reconstruction fidelity than the sequential architecture. We find that the RMSE of reconstructed images reduces significantly for $K > 1$ imagers. PCA offers the best reconstruction fidelity for measuring small M at all noise levels, and also for large M at very low noise level. At high noise levels, e.g., $\sigma_0 > 0.1$, both PCA and Hadamard features perform equally well in terms of minimum RMSE. At moderate noise levels measuring Hadamard features is beneficial.

We also analyze the lifetime of a distributed sensor network. A simple communication protocol is assumed and data sheets from commercially available hardware are used to calculate energy consumption in the system. We compare energy consumption and lifetime of a DFSI system with those of a DCI system both having the same number of sensors. The measurement, computation, and transmission costs are calculated to obtain the total energy consumption in both systems, and by using these data, lifetimes are determined. The lifetime of the DFSI system is 4.8× that of the DCI system when both systems have 20 imagers, reconstruction RMSE requirement is 6%, and the noise level $\sigma_0 = 0.2$. To validate reconstruction fidelity and lifetime observations from the simulations, we emulate a DFSI system by using an array of 5 conventional cameras deployed in an affine geometry. We observe similar trends in systems performance.

Appendix A. Energy consumption calculation

Here we discuss the computation of three energy consumption components: E_{meas}, E_{proc}, and E_{comm}.

A.1. The measurement energy consumption E_{meas}

In a DCI system, we assume an OmniVision VGA camera chip OV7141 and conventional imaging optics to make an isomorphic measurement of the object. The chip has power consumption of 40mW in active mode and frame rate of 30 fps. Therefore E_{meas} in a DCI system using OV7141 is 1.33 mJ per frame.

The calculation of E_{meas} in a DFSI system is different from that in a DCI system. A Thorlabs high speed silicon detector *DET*10*A* is assumed to collect feature values. Following this detector is a 10-bits analog-to-digital converter (ADC) *TLC*1541 from Texas Instrument Inc. The power consumption of *DET*10*A* is defined as $P = I^{2R}$, where I is the photocurrent of the detector, R is the resistance of the circuit. According to the manual of *DET*10*A*, there is a 1 kΩ equivalent resistor in the detector and a recommended 50Ω load resistor. We assume an average photocurrent I is 0.1 mA for visible light. Using the same data sampling rate of 30 fps as in the DCI system, the energy consumption for measuring one feature using a *DET*10*A* detector is 0.35 μJ. Adding the ADC energy consumption from its data sheet, the total energy used to measure one feature in DFSI system is 0.5375 μJ. If one FS imager measures L features, then E_{meas} for one FS imager is $0.5375L$ μJ.

A.2. The on-board processing energy consumption E_{proc}

E_{proc} is the energy required for compressing the measurements. We assume an *ARM*7*TDMI* microprocessor for implementing data compression in both systems. The time period for accomplishing 1 multiplication, addition, and comparison each is 4, 1, and 1 microprocessor operation clock cycles, respectively. The energy used in one clock cycle is 50 pJ. In a DCI system, we use JPEG standard [27,28] for data compression. The DCT-based compression in JPEG standard consists of 8 × 8 DCT transformation, quantization and Huffman coding. According to Prisch et al. [29], the computation requirement for $l \times l$ DCT is log_{2l} multiplications and $2log_{2l}$ additions for each pixel using the fast algorithm. The computation cost for quantization is 1 multiplication per pixel. Therefore, the energy for accomplishing 8 × 8 DCT transformation and quantization process for a $\sqrt{N} \times \sqrt{N}$-pixel object is (3 (multiplication) × 4 + 6 (addition) + 1(multiplication) × 4) × N × 50 = 1100N pJ. The Huffman coding procedure is basically a search procedure over a lookup table. On average half of the table or 80 elements will be searched to code one non-zero DCT coefficient [28]. Therefore, the energy consumed for Huffman coding a $\sqrt{N} \times \sqrt{N}$-pixel object is $4000N\xi$ pJ, where ξ is the compression quality varying from 0 to 1. Now we can formulate E_{proc} for one imager in DCI system as $(1100N + 4000N\xi)$ pJ.

In a DFSI system, the measured data are feature values or transformation coefficients directly. Therefore, transformation computation is saved in the DFSI system. However, the feature values need to be quantized and coded before transmission. Fig. 10 shows the proposed compression protocol for DFSI system. We use the same Huffman coding procedure as in JPEG. The quantization tables $\mathbf{Q}$ are designed individually for each transformation. For DCT features, we interpolate the 8 × 8 DCT quantization table $\mathbf{Q}_8^{DCT}$ in JPEG to generate the 32 × 32 quantization table $\mathbf{Q}_{32}^{DCT}$. For PCA and Hadamard features, we design the quantization tables $\mathbf{Q}_{32}^{PCA}$ and $\mathbf{Q}_{32}^{Hadamard}$ based on the eigen-values of $\mathbf{R}_{\mathbf{x}}$. E_{proc} for one FS imager in a DFSI system is defined as $(200L + 4000\alpha)$ pJ, where α is the number of non-zeros coefficients after compression.

A.3. The communication energy consumption E_{comm}

E_{comm} is modeled as $E_{comm}(\gamma, d) = E_{elec}\gamma + \varepsilon_{amp}\gamma d^2$, where E_{elec} = 50 nJ/bit is the radio dissipate, $\varepsilon_{amp} = 100\text{pJ}/(\text{bit} \cdot \text{m}^2)$ is for the transmitter amplifier, γ is the number of data bits transmitted, and d is the transmission distance [30]. All imagers are assumed 1 km away from the base station. Therefore to transmit γ data bits, E_{comm} is $100,050\gamma$nJ.

Table 3 summarizes the device part numbers and energy consumption values for DCI and DFSI systems.

References

[1] Y. Sankarasubramaniam, I. Akyildiz, W. Su, E. Cayirci, IEEE Communication Magazine 40 (2002) 102.
[2] M. Rahimi, Y. Yu, D. Estrin, G.J. Pottie, M. Srivastava, G. Sukhatme, R. Pon, M. Batalin W.J. Kaiser, in: Proceedings 10th IEEE International Workshop on Future Trends of Distributed Computing Systems, 2004, p. 102.
[3] S. Hengstler, H. Aghajan, in: Testbeds and Research Infrastructures for the Development of Networks and Communities, IEEE, 2006.
[4] W. Feng, W. Feng, E. Kaiser, M. Baillif, Communications and Applications 1 (2005) 151.
[5] Y. Liu, S. Das, IEEE Communication Magazine 44 (2006) 142.
[6] S. Hengstler, H. Aghajan, ACM/IEEE International Conference on Distributed Smart Cameras 1 (2007) 12.
[7] E. Culurciello, A.G. Andreou, Analog Integrated Circuits and Signal Processing 49 (2006) 39.
[8] D. Ganesan, G. Mathur, P. Desnoyers, P. Shenoy, in: Proceedings of the Fifth International Conference on Information Processing in Sensor Networks, 2006, p. 374.
[9] M.W. Marcellin, J.C. Dagher, M.A. Neifeld, IEEE Transaction on Image Processing 15 (2006) 1705.
[10] C. Duran-Faundez, V. Lecuire, N. Krommenacker, EURASIP Journal on Image and Video Processing (2007) 1.
[11] A. Savvides, E. Culurciello, in: 2nd International Conference on Broadband Networks. IEEE, 2005.
[12] M.A. Neifeld, P.M. Shankar, Feature Specific Imaging Applied Optics 42 (2003) 3379.
[13] H. Pal, M.A. Neifeld, Optics Express 11 (2003) 2118.
[14] H. Pal, D. Ganotra, M.A. Neifeld, Applied Optics 44 (2005) 3784.
[15] M.A. Neifeld, J. Ke, Applied Optics 46 (2007) 5293.
[16] J. Ke, M. Stenner, M.A. Neifeld, in: Proceedings of SPIE, Visual Information Processing XIV, vol. 5817. SPIE, 2005.
[17] D.J. Brady, N.P. Pitsianis, X. Sun, in: Proceedings of SPIE, Visual Information Processing XIV, vol. 5817. SPIE, 2005.

[18] A. Portnoy, X. Sun, T. Suleski, M.A. Fiddy, M.R. Feldman, N.P. Pitsianis, D.J. Brady, R.D. TeKolste, in: Proceedings of SPIE, Intelligent Integrated Microsystems, vol. 6232. SPIE, 2006.
[19] D. Donoho, IEEE Transaction on Information Theory 52 (2006) 1289.
[20] J.K. Romberg, E.J. Candes, Proceedings of SPIE, Wavelet Applications in Signal and Image Processing XI, vol. 5914. SPIE, 2004.
[21] E.J. Candes, in: Proceedings of the International Congress of Mathematicians, 2006.
[22] J.A. Tropp, IEEE Transactions on Information Theory 50 (2004) 2231.
[23] D. Takhar, J. Laska, T. Sun, K. Kelly, M. Duarte, M. Davenport, R. Baraniuk, To appear in IEEE Signal Processing Magazine (2008).
[24] K. Dasgupta, K. Kalpakis, P. Namjoshi, Computer Networks 42 (2003) 697716.
[25] V. Paciello L. Ferrigno, S. Marano, A. Pietrosanto, in: IEEE International Conference on Virtual Environments, Human–Computer Interfaces, and Measurement Systems, 2005.
[26] A. Goshtasby, Image Visbile Computation 6 (1988) 255.
[27] G.K. Wallace, Communications of the ACM 34 (1991) 30.
[28] CCITT. Information technology – digital compression and coding of continuous-tone still images – requirements and guidelines. ISO/IEC 10918-1:1993(E).
[29] N. Demassieux, P. Pirsch, W. Gehrke, Proceedings of the IEEE 83 (1995) 220.
[30] S.S. Iyengar, R.R. Brooks, Distributed Sensor Networks, Chapman & Hall/CRC, 2005.